sustainability

MDPI

Article

# The Effect of Recycled Sand on the Tensile Properties of Engineered Cementitious Composites

**Zhifu Dong [1,2], Yan Tan [1], Xiangru Jian [2], Jiangtao Yu [1,2,*] and Kequan Yu [2]**

1 School of Civil Engineering, Architecture, and Environment, Hubei University of Technology, Wuhan 430068, China
2 College of Civil Engineering, Tongji University, Shanghai 200092, China
* Correspondence: yujiangtao@tongji.edu.cn

**Abstract:** This research aims to investigate the feasibility of replacing natural sand (NS) with recycled sand (RS) to enhance the mechanical property of engineered cementitious composites (ECC). For a comparative study, ECCs incorporating natural sands (NS) and recycled sands with different sieve sizes were taken as experimental subjects. The results demonstrated that RS-ECC possessed better tensile properties featuring saturated cracks and superior strain-hardening behavior than that of NS-ECC. The highest tensile strain capacity of RS-ECC was up to 7%. Meanwhile, the compressive and flexural strengths of RS-ECC were over 50 and 20 MPa. The pseudo-strain-hardening (PSH) index of the RS-ECC-20 grid and RS-ECC-12 grid were 141 and 201, which increased by 46% and 70% than that of NS-ECC. Furthermore, the thicker weak ITZ and comparatively aggregate/ITZ ratio were found in the RE-ECC by a microstructure test, which revealed and explained the mechanism for the lower matrix fracture toughness of RS-ECC.

**Keywords:** engineered cementitious composites; recycled sand; strain-hardening behavior; tensile strain capacity; fracture toughness

check for updates

**Citation:** Dong, Z.; Tan, Y.; Jian, X.; Yu, J.; Yu, K. The Effect of Recycled Sand on the Tensile Properties of Engineered Cementitious Composites. *Sustainability* **2022**, *14*, 13530. https://doi.org/10.3390/su142013530

Academic Editor: Enzo Martinelli

Received: 26 July 2022
Accepted: 17 October 2022
Published: 19 October 2022



## 1. Introduction

Concrete is the largest artificial material used in civil engineering at present. The production of concrete consumes an enormous amount of fine aggregate, e.g., river sand and manufactured sand. The overexploitation of river sand brings a series of environmental problems. Hence, some governments in the world have issued rules to limit sand mining from rivers, e.g., the No. 320 Decree in China [1]. Manufactured sand is generally made from crushing stone by artificial processes. Besides consuming natural resources, the production of manufactured sand is considered to generate considerably large $CO_2$ emissions [2,3]. Meanwhile, construction and demolition (C&D) waste, produced by demolishing abandoned structures, takes a relatively large proportion of the total amount of waste in recent years. The most common disposal method of C&D waste in some developing countries is landfilled, inevitably resulting in water, atmospheric and soil contamination as well as landfill saturation [4,5]. Using C&D waste to produce recycled construction materials, e.g., recycled aggregate, is a reasonable method to minimize the negative influence on end-of-life structures, as well as to decrease the demand for extraction of resources. In processing C&D waste, recycled sand (RS) accounts for about 20% of the gross amount of recycled aggregate [6–9]. Despite RS being abundant in C&D waste, the understanding of concrete incorporated with RS is limited. In recent years, many investigators have attempted to investigate the influence of RS replacement on the mechanical property of concrete. Khatib [10] conducted a series of experiments to investigate the replacement ratios of fine recycled aggregate (FRA) on the mechanical property, which led to 15% and 30% compressive loss at replacement ratios of 25% and 100%, respectively. Evangelista et al. [11] stated that there were no significant reductions with percentages of substitution of RS up to 30%. Khoshkenari et al. [12] discovered that FRA decreases the splitting tensile and compressive strength of concrete, which can be compensated by incorporating fine natural aggregate of 0–2 mm size. Pereira et al. [13] demonstrated that the mechanical properties of the concrete prepared from RS incorporated with superplasticizer exceeded that of normal concrete in the control group. Huang et al. [14] introduced two kinds of RS with different crashing processes and fine moduli into concrete. The test results indicated that RS with a small fine modulus and low water absorption rate tends to help maintain the mechanical strength of concrete.

With all the research achievements above, the application of RS in producing concrete is still limited, due to its unique physical property that leads to relatively weak strength and poor workability [15]. However, the weakness of RS might be an advantage when RS is used as fine aggregate for producing fiber-reinforced cementitious composites, specifically, engineered cementitious composites (ECC) [16,17]. ECC, also named strain-hardening cementitious composites (SHCC) [18,19], belong to the fiber-reinforced cementitious composites, which exhibit pseudo strain-hardening behavior with excellent tensile properties and crack width less than 100 mm [20,21]. Based on the above advantage, ECC overcomes many of the challenges associated with the brittleness and cracking of concrete materials, improving the safety and durability of infrastructure [22–26]. Nevertheless, there are still some limitations in the research and development of ECC, such as how to further enhance the tensile ductility. According to the pseudo-strain-hardening (PSH) index proposed by Kanda and Li [27], the tensile strain capacity of ECC is basically proportional to the ratio of fiber bridging capacity and fracture toughness of the matrix. To guarantee the stability of the strain-hardening property, the fracture toughness would maintain a relatively low level. For this reason, some kinds of special aggregates, such as crumb rubbers, geopolymer, were introduced into the system of ECC as flaws to further lower the matrix fracture toughness [28–31]. The RS mentioned above can also be classified as this kind of aggregate. In addition, incorporating it into ECC can realize the recycling of waste and reduce the impact on the environment. Based on the considerations, the authors tried to replace the natural sand (NS) with RS to improve the mechanical properties of ECC. With the above points in mind, the main objectives of this research are summarized as follows:

- Achieve a better understanding of recycled sand applicable to ECC. X-ray fluorescence (XRF), scanning electron microscope (SEM) and particle size analysis were used to obtain chemical compositions, physical properties, and fineness of RS.
- Investigate the influence of RS replacement on the basic mechanical properties of ECC.
- Find the influence of RS replacement on the meso-scale and micro-scale properties of RS-ECC and explore the connection between the RS-ECCs tensile strain capacity and meso-scale property.

## 2. Materials and Experimental Program

### *2.1. Materials and Mix Proportions*

The mixture proportions of the ECC used for the study are presented in Table 1. The mixture proportions differ from each other in RS content or sieve size. Specifically, in two reference mixtures, i.e., NS-ECC-12 grid and NS-ECC-20 grid (NS-ECC), NS with sieve size 12 grid and 20 grid were added as fine aggregate, respectively. In RS-ECC-12 grid and RS-ECC-20 grid, all contents of the NS were replaced by RS with corresponding particle sizes. In all the mixtures, the binder includes P.II 52.5 Portland cement and class F fly ash. Table 2 lists the chemical compositions of cement, fly ash, and RS, which were acquired by XRD analysis. A set of sieves was employed to obtain the particle size distribution of RS and NS used in the mixture. Figure 1 illustrates the analysis results. Due to the relatively high water absorption of RS, a more high-range water reducer (HRWR) was applied in mixing RS-ECC to ensure workability, as shown in Table 1. Ultra-high molecular weight polyethylene (PE) fibers were used as reinforcement in all the mixtures with a constant volume fraction of 2%. The property of PE is presented in Table 3.

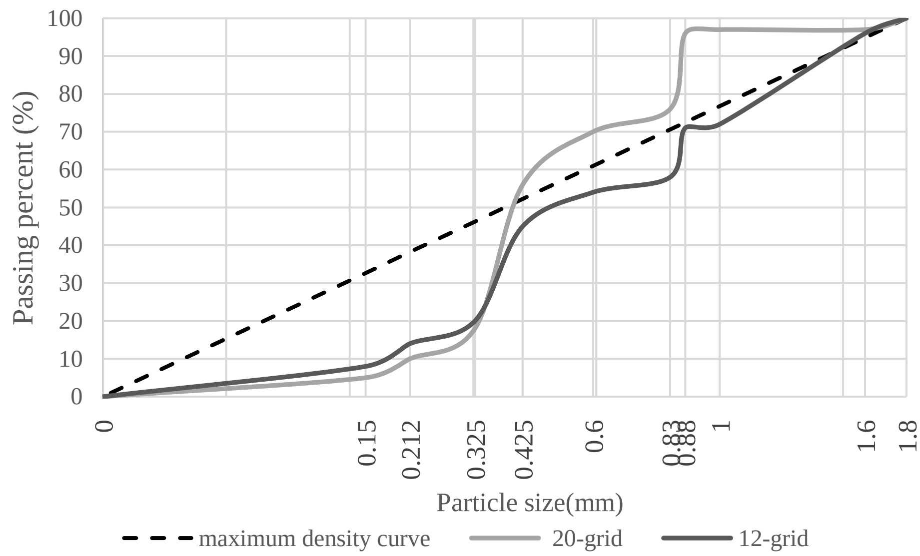


**Figure 1.** Particle size of sand used in mixtures.

**Table 1.** Mixture proportion of ECC (kg/m$^3$).

| Mixture ID | PE Fiber (g) | Cement (g) | Fly Ash (g) | NS (g) | RS (g) | Water (g) | HRWR (g) |
|---|---|---|---|---|---|---|---|
| RS-ECC-20 grid | 20 | 628 | 754 | 0 | 502 | 387 | 1.8 |
| RS-ECC-12 grid | 20 | 628 | 754 | 502 | 0 | 387 | 1.0 |
| NS-ECC-20 grid | 20 | 628 | 754 | 0 | 502 | 387 | 1.8 |
| NS-ECC-12 grid | 20 | 628 | 754 | 502 | 0 | 387 | 1.0 |

**Table 2.** Chemical compositions of raw materials (wt.%).

| Ingredients | | Fly Ash | Recycled Sand |
|---|---|---|---|
| **Chemical composition (%)** | $Na_2O$ | 0.58 | 0.86 |
| | MgO | 0.90 | 2.26 |
| | $Al_2O_3$ | 23.9 | 12.0 |
| | $SiO_2$ | 51.7 | 47.9 |
| | $P_2O_5$ | 0.40 | 0.29 |
| | $SO_3$ | 0.91 | 1.41 |
| | $K_2O$ | 1.40 | 2.33 |
| | CaO | 7.65 | 18.7 |
| | $TiO_2$ | 1.19 | 0.82 |
| | MnO | 0.07 | 0.10 |
| | $Fe_2O_3$ | 5.22 | 6.53 |
| | $Cl^-$ | / | 0.06 |
| | $Cr_2O_3$ | / | 0.02 |
| | NiO | / | 0.01 |
| | CuO | / | 0.01 |
| | ZnO | / | 0.02 |
| | SrO | / | 0.03 |
| | $ZrO_2$ | / | 0.02 |

**Table 3.** Properties of PE fiber.

| Diameter (µm) | Fiber Aspect Ratio | Nominal Strength (GPa) | Modulus (GPa) | Rupture Elongation (%) | Density (g/cm$^3$) | Melting Point (°C) |
|---|---|---|---|---|---|---|
| 25 | 720 | 2.9 | 116 | 2.42 | 0.97 | 150 |

### 2.2. Preparation of Specimens

All the mixtures were mixed in a 20 L mixer. The binder and water were continuously mixed for 2 min. HRWR was added into the mixer and mixed to reach proper mortar fluidity. Finally, fibers were added by hand and mixed for 2 min to ensure fiber dispersion well. Afterward, the fresh ECC was cast into molds. All specimens were demolded after 24 h and then cured in the air for another 27 days.

### 2.3. Mechanical Properties Tests

The test scheme is presented in Table 4, listing the number of specimens in each test case.

**Table 4.** Experimental test scheme (specimen number).

| Mixture ID | RS-ECC-12 Grid | NS-ECC-12 Grid | RS-ECC-20 Grid | NS-ECC-20 Grid |
|---|---|---|---|---|
| Uniaxial tension test | 12 | 12 | 12 | 12 |
| Uniaxial compression test | 6 | 6 | 6 | 6 |
| Uniaxial compression test (mixture without fiber) | 6 | 6 | 6 | 6 |
| Single crack tension test | 6 | 6 | 6 | 6 |
| Three-point bending test | 3 | 3 | 3 | 3 |
| Three-point bending test (mixture without fiber) | 3 | 3 | 3 | 3 |
| Fracture toughness test (mixture without fiber) | 3 | 3 | 3 | 3 |

Dog-bone plates (Figure 2) were adopted as specimens for uniaxial tension tests. A WDW-300Y electro-servo machine (1 N resolution) was employed to apply displacement–control loading with a uniform rate of 1.5 mm/min. Two linear variable displacement transducers (LVDTs) were installed on both sides of the specimen to obtain the displacement of specimens, and the gauge length was 80 mm.

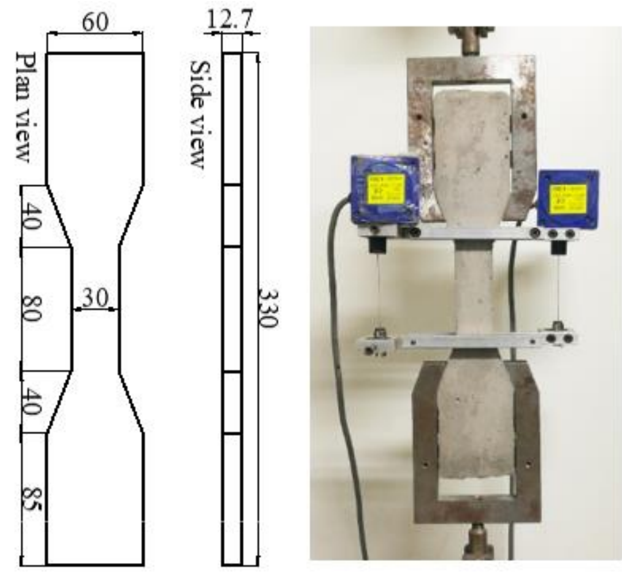


**Figure 2.** Dog-bone specimen for RS-ECC tensile test (Note: All dimensions in mm).

Six cubic specimens of every mixture were prepared to assess the compressive property of RS-ECC. The size of the geometric dimension was 40 × 40 × 40 mm. The test procedure is according to the GB/T 50081-2016.

Three-point bending tests were also applied to prism specimens of every mixture in an MTS 244 electro-hydraulic servo machine. The geometric dimension of the prism specimens was 40 × 40 × 160 mm. The test procedure is according to the GB/T 50081-2016. To obtain full-field deformation, the digital image correlation (DIC) method was used for acquiring the deformation of specimens of normal composites (with fiber).

Single-crack tensile tests were conducted to examine the interfacial strength between the fiber and matrix. In Figure 3, two symmetrical notches with a width less than 0.6 mm were cut by an ultra-thin saw blade (0.4 mm in thickness), which is conducive for a single crack to form. Figure 4 illustrates the geometric size of the specimen. To avoid excrescent cracks forming inside or outside the notches and to ensure an ideal condition that only a single crack will be generated under tensile load, the adopted notched cross-section had an area of 50% of its original value. In Figure 3, the crack opening displacement was measured by a pair of clip-on gauges.

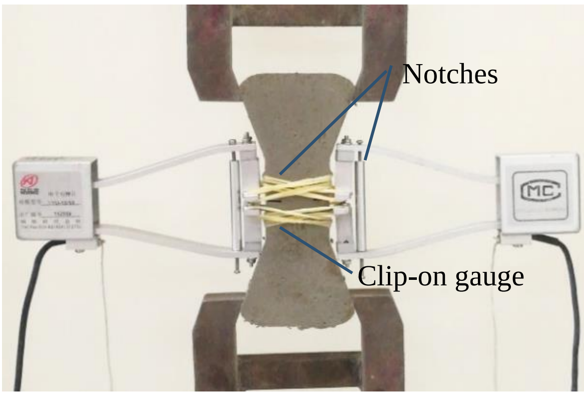


**Figure 3.** Single-crack tension test and instrumentation.

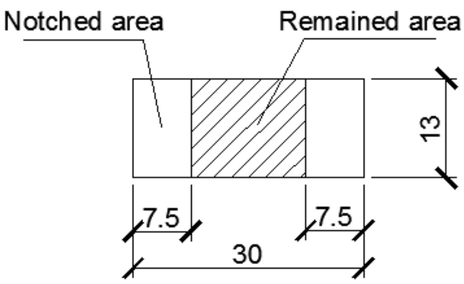


**Figure 4.** Notched cross-section of a minor dog-bone specimen.

Three-point loading tests were conducted to analyze the influence of RS posing on the matrix fracture toughness. The geometry of the notched beam is shown in Figure 5. As shown in Figure 6, a SANSI electro-hydraulic servo machine was applied in the tests, with a displacement–control loading rate of 1.0 mm/minute. To reveal the formation of different fracture toughness between RS-ECC and NS-ECC, a 3D-shape measurement test and nanoindentation test were performed on the fracture surfaces of the notched beams after bending tests. The 3D shape measurement instrumentation with grating projection, as shown in Figure 7, was used to obtain the photo of the fracture surface. The mechanism of the instrument is that two symmetrical projectors project the grating on the fracture surface, which will be received by the camera after diffuse reflection on the surface. The altitude of every point on the surface can be obtained by analyzing the transformation of the grating, mainly the change in the width of the stripes. Combining it with the plain coordinates of points, 3D coordinate matrices of the fracture surface were obtained.

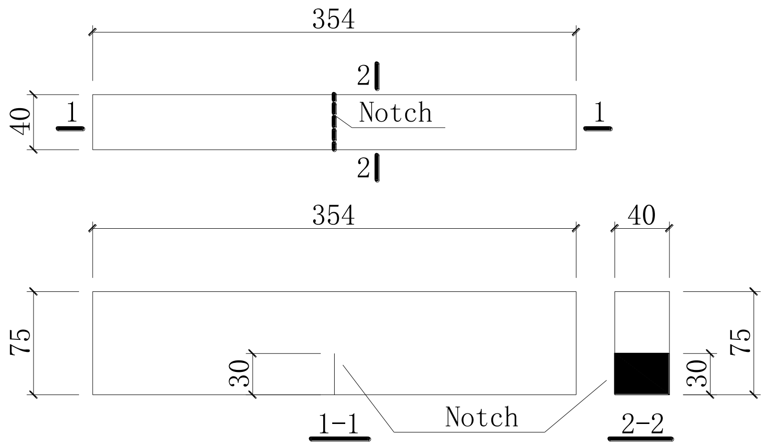


**Figure 5.** Geometry of notched beam.

**Figure 6.** Fracture toughness test on RS-ECC matrix.


**Figure 7.** Three-dimensional shape measurement instrumentation.

The nano-indentation tests were conducted by using the Hysitron Triboindenter fitted with a Berkovitch tip. The loading process had a loading rate of 300 μN/s, maintaining a constant force of 1.5 mN for 2 s, and an unloading rate of 300 μN/s. The analytical Oliver and Pharr method were used to calculate the indentation hardness and elastic modulus of sands, interfacial transition zone (ITZ), and cement matrix of ECC.

## 3. Results and Discussions

### 3.1. Tensile Behavior

Figure 8 exhibits the residual crack pattern of all four mixtures. The number of cracks in the 80 mm gauge length was counted after the test. Based on the crack numbers and the obtained tensile deformation at peak strength, the average crack width and crack spacing were calculated. Table 5 shows the average values. The crack numbers of RS-ECC, i.e., 44.5 of 20 grid and 37.1 of 12 grid, are larger than those of NS-ECC, i.e., 29.7 of 20 grid and 26.4 of 12 grid, implying the better multi-cracking characteristic of RS-ECC. Meanwhile, the RS-ECC might possess fine penetration resistance and excellent durability even under extreme stretching [32], since the crack widths of RS-ECC of both 20 grid and 12 grid are smaller than those of NS-ECC. When comparing the effect of particle size on crack behavior (Table 5), it is seen that the mixture with 20 grid sand has better performances in both tensile strain capacity and crack distribution than the one with 12 grid, which is compliant with the idea that a larger size of aggregate in ECC leads to lower mechanical property [33].

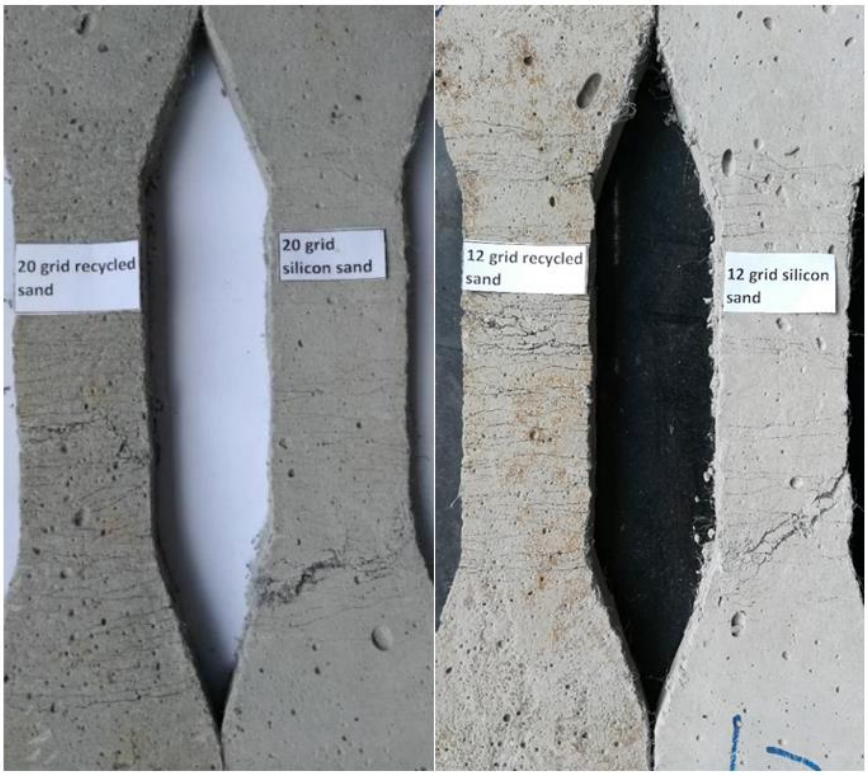


**Figure 8.** Surface appearances of RS-ECC after tension.

**Table 5.** Crack width and spacing at failure.

| Mixture ID | Crack Number (80 mm) | Crack Width (μm) | Crack Spacing (mm) |
|---|---|---|---|
| RS-ECC-20 grid | 44 | 117 | 1.93 |
| RS-ECC-12 grid | 37 | 119 | 2.16 |
| NS-ECC-20 grid | 29 | 125 | 2.69 |
| NS-ECC-12 grid | 26 | 145 | 3.03 |

Figure 9 and Table 6 present the summaries for the tensile properties of the tested specimens. The average peak tensile strength of the RS-ECC-20 grid, RS-ECC-12 grid, NS-ECC-20 grid, and NS-ECC-12 grid were 4.75, 4.18, 3.96, and 3.86 MPa, respectively. RS-ECC had better tensile strength than NS-ECC. Meanwhile, the average tensile strain at the peak strength of those four mixtures reached 7.00%, 5.52%, 4.64%, and 4.78%, respectively, indicating again the better multi-cracking behavior of RS-ECC. The peak tensile stress over the first cracking stress ratios is presented in Table 6. This ratio of RS-ECC was also a bit larger than that of NS-ECC and they all surpassed two 2 on average. Combining these three aspects, it could be concluded that RS-ECC has a relatively strong strain-hardening characteristic that enables it to have both superior tensile strain capacity and strength.

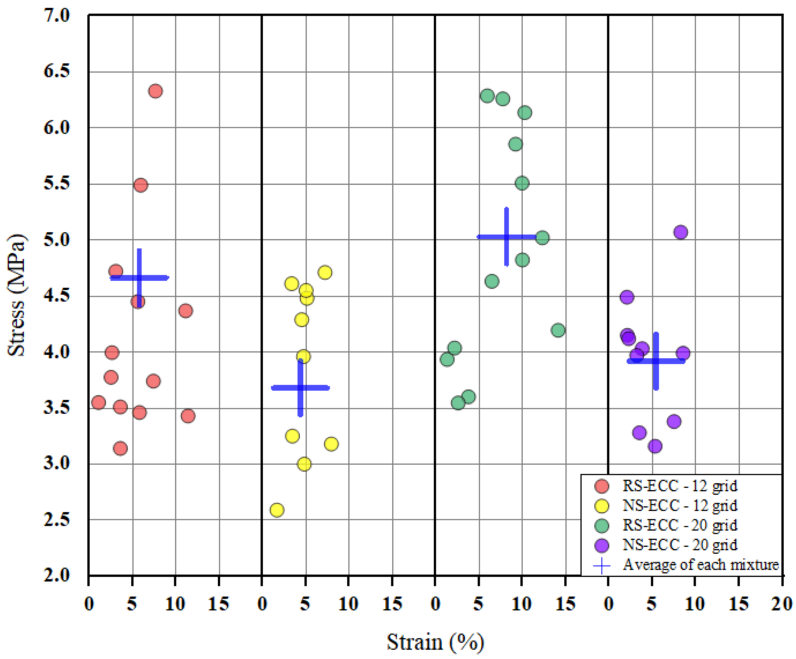


**Figure 9.** Scatter figure of results of uniaxial tension test.

**Table 6.** Results of uniaxial tension test (average value).

| Mixture ID | First Cracking Stress (N/mm$^2$) | Cracking Strain (%) | Peak Tensile Stress (N/mm$^2$) | Strain at Peak Stress (%) | Peak Tensile Stress/First Cracking Stress | Strain at 85% of the Peak Stress (%) |
|---|---|---|---|---|---|---|
| Normal ECC | 1.68 | 0.02 | 4.27 | 4.76 | 2.54 | 7.22 |
| RS-ECC-20 grid | 2.21 | 0.08 | 4.75 | 7.00 | 2.15 | 8.22 |
| RS-ECC-12 grid | 2.03 | 0.07 | 4.18 | 5.52 | 2.06 | 6.73 |
| NS-ECC-20 grid | 1.97 | 0.03 | 3.96 | 4.64 | 2.01 | 5.32 |
| NS-ECC-12 grid | 1.88 | 0.02 | 3.86 | 4.78 | 2.05 | 5.88 |

From the scatter plot in Figure 9, the tensile property of RS-ECC has a larger variance, although it behaves better in all aspects of the tensile test on average. In addition, even using the same kind of sand, the mixture with finer sand had a smaller variance than the one with a coarser one. This might be the result of the effect that the fineness and shape of the aggregate pose on the dispersion of the fiber. Generally, the finer aggregate leads to more even fiber dispersion [33]. Furthermore, the irregular morphology of RS, as shown in Figure 14, may lead to uneven and unstable distribution, which attributes to the large deviation of tensile behavior of RS-ECC.

### *3.2. Compressive and Bending Properties*

Table 7 summarizes the results of all the uniaxial compression and three-point bending tests. Mixture ID including plain in Table 7 refers to the specimens without fiber. The average peak uniaxial compression stresses were 35.91 MPa for the RS-plain-20 grid and 42.50 MPa for the RS-plain-12 grid, which were similar to their NS counterparts in magnitude. The flexural strength of the RS-plain 20 grid and RS-plain 12 grid was 7.55 and 7.43 MPa, slightly lower than the NS-plain 20 grid and NS-plain 12 grid, which was 8.87 and 8.86 MPa, respectively. Combining the results of both tests, a conclusion can be drawn that RS replacement decreases the mechanical properties of concrete if no fiber reinforcement is incorporated.

**Table 7.** Results of compression and bending test (average).

| Mixture ID | Peak Compressive Strength (MPa) | Peak Flexural Strength (MPa) | Mid-Span Deformation at Peak Flexural Strength (mm) |
|---|---|---|---|
| RS-plain-20 grid | 35.91 | 7.55 | / |
| RS-plain-12 grid | 42.50 | 7.43 | / |
| NS-plain-20 grid | 40.91 | 8.87 | / |
| NS-plain-12 grid | 38.66 | 8.86 | / |
| RS-ECC-20 grid | 54.86 | 21.10 | 7.37 |
| RS-ECC-12 grid | 53.65 | 20.65 | 4.45 |
| NS-ECC-20 grid | 74.73 | 24.87 | 3.65 |
| NS-ECC-12 grid | 52.88 | 24.40 | 5.89 |

Table 7 shows the compressive and flexural strength of materials reinforced with fibers. Comparing the test results of RS-ECC to NS-ECC, the compressive strength of the NS-ECC-20 grid, i.e., 74.73 MPa, is obviously larger than the other composites, not only indicating that both fineness and type of sand will influence the compressive strength but also proving the factor of fineness weights over the type.

Similar to the result of the ECC matrix, the flexural strength of RS-ECC is also slightly smaller than that of NS-ECC. Moreover, the deformations at the midspan of RS-ECC measured by the DIC method are significantly larger than those of NS-ECC, indicating a better multi-cracking behavior and strain-hardening effect that is consistent with the results obtained in the uniaxial tensile test; see Figure 10. To give a clearer view, one typical load–deformation curve of each mixture case is presented in Figure 11. It is well observed that more cracks were generated throughout the test process on RS-ECC specimens, especially the 20 grid mixture case.

In summary, the mechanical strength of RS-ECC is close to or slightly smaller, but the tensile strain capacity and flexural deformability of RS-ECC are significantly improved as compared with those of NS-ECC. To explore the underlying reason, further analyses were conducted at the meso-scale, as shown in the following section.

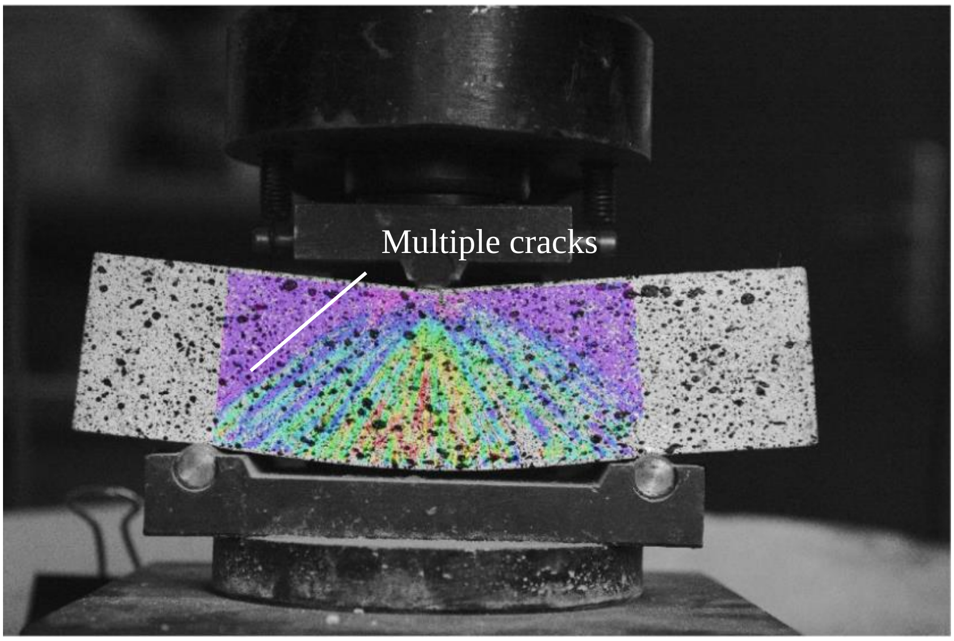


**Figure 10.** Contour map of deformation of RS-ECC−20 grid using DIC.

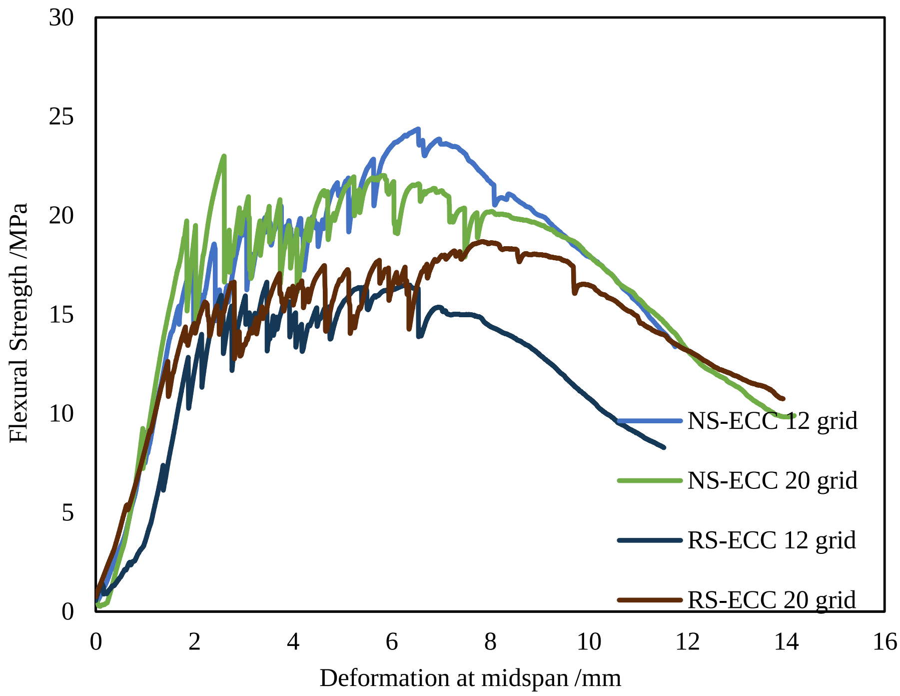


**Figure 11.** Flexural strength vs. deformation of the three-point bending beams.

### *3.3. Discussion on the Effect of RS Replacement at the Meso-Scale*

The typical stress vs. crack mouth opening displacement (CMOD) curves of the single crack tensile test are illustrated in Figure 12. In Equation (1), the complementary energy $J_b{}'$ is computed from the hatched area, as shown in Figure 12. $J_b{}'$ reflects the energy consumed when fibers are pulled out from the matrix. The CMOD curves of the four mixtures are shown in Figure 13. The different colored lines in Figure 13 demonstrate the different specimens in each groups. Table 8 lists the key parameters of the test.

$$J_b' = \sigma_{B,\max}\delta_B - \int_0^{\delta_B} \sigma_B(\delta)d\delta \quad (1)$$

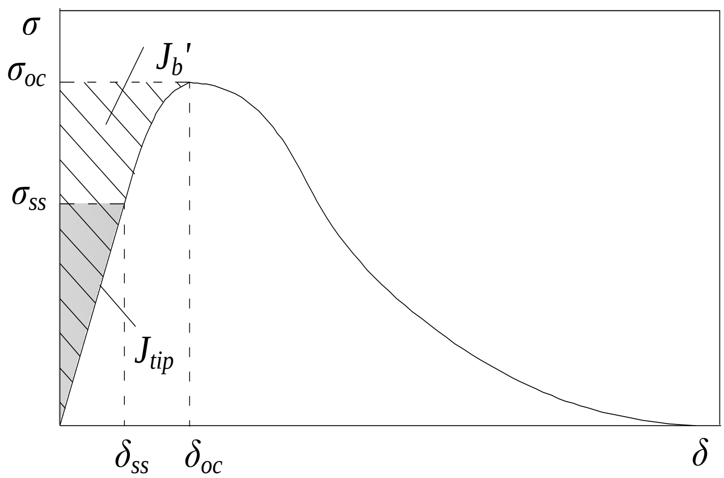


**Figure 12.** Typical $\varsigma$-$\delta$ curve for strain-hardening composites. The hatched area represents complementary energy $J_b{}'$. Shaded area represents matrix toughness $J_{tip}$.

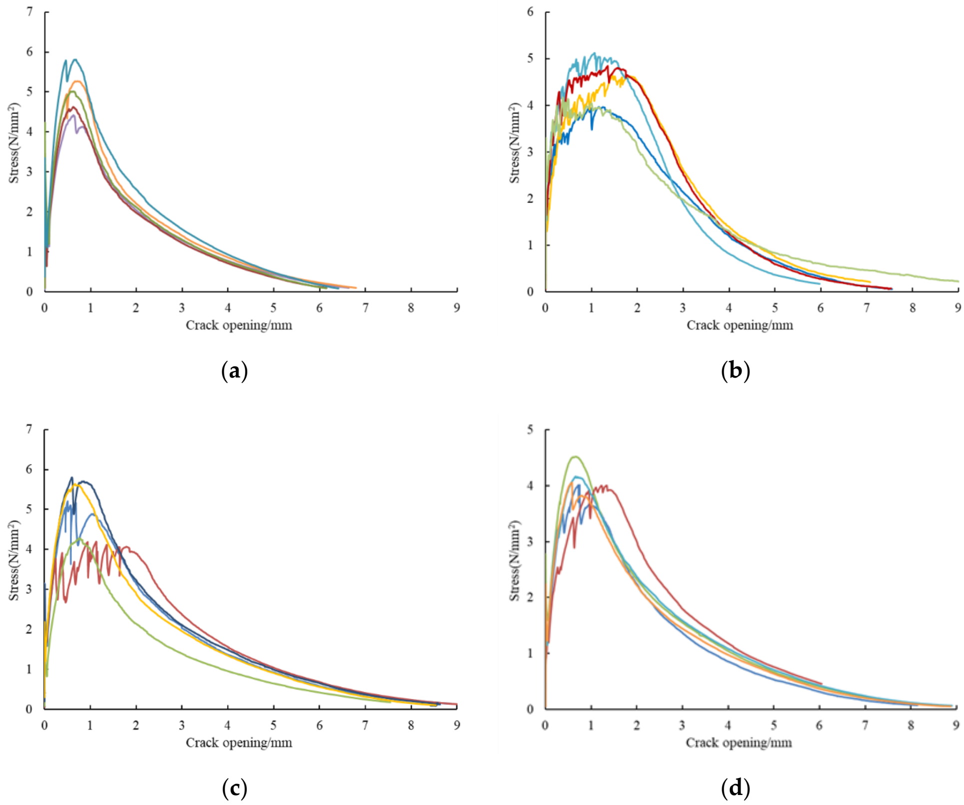


**Figure 13.** Single crack tensile test curve of ECC mixtures. (**a**) RS-ECC-20 grid; (**b**) RS-ECC-12 grid; (**c**) NS-ECC-20 grid; (**d**) NS-ECC-12 grid.

**Table 8.** Test results of single-crack tension test.

| Mixture ID | Parameter | Average | Variance |
|---|---|---|---|
| RS-ECC-20 grid | $\sigma_{OC}$ (Mpa) | 4.32 | 0.12 |
| | $\delta_B$ (mm) | 0.81 | 0.07 |
| RS-ECC-12 grid | $\sigma_{OC}$ (Mpa) | 5.02 | 0.45 |
| | $\delta_B$ (mm) | 0.73 | 0.05 |
| NS-ECC-20 grid | $\sigma_{OC}$ (Mpa) | 4.55 | 0.18 |
| | $\delta_B$ (mm) | 1.08 | 0.14 |
| NS-ECC-12 grid | $\sigma_{OC}$ (Mpa) | 5.03 | 0.24 |
| | $\delta_B$ (mm) | 0.65 | 0.00 |

The fiber bridging stress $\sigma_{OC}$ suffered almost no loss when NS was replaced by RS (in Figure 6), which indicates that RS has little adverse effect on the bond-slip capacity between the fiber and matrix.

The fracture toughness $K_Q$ and the fracture energy $J_{tip}$ of the three-point bending tests are calculated by the following equations [34].

$$K_Q = \frac{P_Q S}{\sqrt{BB_N} W^{3/2}} \cdot f\left(\frac{a}{W}\right) \quad (2)$$

$$f\left(\frac{a}{W}\right) = 3\sqrt{\frac{a}{W}} \cdot \frac{1.99 - \left(\frac{a}{W}\right)\left(1 - \frac{a}{W}\right)\left[2.15 - 3.93\frac{a}{W} + 2.7\left(\frac{a}{W}\right)^2\right]}{2\left(1 + 2\frac{a}{W}\right)\left(1 - \frac{a}{W}\right)^{3/2}} \quad (3)$$

$$J_{tip} = K_Q^2 / E_m \quad (4)$$

The $K_Q$ and $J_{tip}$ are listed in Table 9. The average fracture toughness of the RS-plain-20 grid and RS-plain-12 grid was 0.393 and 0.363 MPa·m$^{1/2}$, obviously lower than that of the NS-plain-20 grid and NS-plain-12 grid, which was 0.514 and 0.463 MPa·m$^{1/2}$, respectively. In comparison to NS, RS has the ability to reduce the matrix fracture toughness. When focusing on the effect on fracture energy brought by fineness of the aggregate, it is well known that finer aggregate leads to smaller fracture energy [35]. Consistently, specimens of the 20 grid had smaller fracture energy, as compared to those of the 12 grid.

**Table 9.** Fracture toughness of ECC matrix.

| Mixture ID | Specimen | Mass (kg) | Peak Load $F_Q$ (kN) | Fracture Toughness $K_Q$ (MPa·m$^{1/2}$) | Fracture Energy $J_{tip}$ (J/m$^2$) |
|---|---|---|---|---|---|
| RS-plain-20 grid | 1 | 2.02 | 0.55 | 0.43 | 11.44 |
| | 2 | 2.10 | 0.44 | 0.34 | 7.29 |
| | 3 | 1.98 | 0.53 | 0.41 | 10.53 |
| | Average | 2.03 | 0.51 | 0.39 | 10.99 |
| RS-plain-12 grid | 1 | 2.02 | 0.45 | 0.35 | 7.47 |
| | 2 | 2.01 | 0.52 | 0.40 | 9.96 |
| | 3 | 1.98 | 0.45 | 0.35 | 7.44 |
| | Average | 2.00 | 0.52 | 0.36 | 8.29 |
| NS-plain-20 grid | 1 | 2.06 | 0.63 | 0.50 | 14.92 |
| | 2 | 2.15 | 0.67 | 0.52 | 16.92 |
| | 3 | 2.09 | 0.69 | 0.53 | 17.68 |
| | Average | 2.10 | 0.67 | 0.51 | 16.51 |
| NS-plain-12 grid | 1 | 2.07 | 0.59 | 0.46 | 12.96 |
| | 2 | 2.13 | 0.59 | 0.46 | 12.96 |
| | 3 | 2.10 | 0.62 | 0.48 | 14.27 |
| | **Average** | **2.10** | **0.60** | **0.47** | **13.40** |

To combine two aspects into one parameter that can measure the strain-hardening effect of a certain kind of composite, according to the pseudo-strain-hardening (PSH) index [27], the tensile strain capacity of cementitious composites is tightly associated with the fiber bridging complementary energy $J_b'$ and the matrix fracture energy $J_{tip}$. To be more specific, a relatively lower ratio of $J_{tip}/J_b'$ tends to easily lead to crack generation and propagation, which finally facilitate the tensile capacity of the composite. As can be seen in Table 10, the replacement of NS by RS efficiently reduces the fracture toughness of the matrix and keeps the fiber bridging capacity $J_b'$ nearly constant. In addition, it can be concluded that the fracture toughness of the matrix could be reduced by coarse sand (12 grid), not only for RS but also for NS. As a result, the PSH index $J_b'/J_{tip}$ increases by 46% and 70% after the replacement of NS by RS of the 20 and 12 grids, respectively. There is a similar trend between the $J_b'/J_{tip}$ and the tensile ductility. The impact of RS replacement is reflected in the enhanced pseudo-strain-hardening (PSH) index $J_b'/J_{tip}$, therefore explaining the positive influence of RS on the tensile strain capacity of ECC.

**Table 10.** Comparisons on PSH index.

| Mixture ID | $J_b'$ (J/m$^2$) | $J_{tip}$ (J/m$^2$) | $J_b'/J_{tip}$ (PSH) | $\varepsilon_t$ (%) |
|---|---|---|---|---|
| RS-ECC-20 grid | 1552.15 | 10.99 | 141.23 | 8.22 |
| RS-ECC-12 grid | 1668.61 | 8.29 | 201.28 | 6.73 |
| NS-ECC-20 grid | 1597.55 | 16.51 | 96.76 | 5.32 |
| NS-ECC-12 grid | 1585.17 | 13.40 | 118.30 | 5.88 |

In summary, the enhanced property of RS-ECC is attributed to the reduced fracture toughness of the matrix. According to previous studies, there are two possible explanations for this phenomenon. The first one is due to the different patterns of crack propagation [36,37]. In NS-plain, cracks may bypass the aggregate when it is on the way to crack propagation since the natural sand is too hard and too tough to be torn apart. Therefore, cracks leave a fracture surface with a larger area, which requires more energy. However, it is different in RS-plain because the structure of RS is weaker and thus easier to be torn apart. Thus, the crack can easily go through the aggregate with relatively smaller stress and form a fracture surface with a smaller area. The other reason is the weak nature of the ITZ between the new cement binder and the old mortar on the RS surface [38]. Instead of directly going through sand, the crack needs less stress as well as energy to break the ITZ and tear the sand apart from the cement binder in RS-ECC. Therefore, the fracture toughness and energy of the RS-plain are smaller than those of the NS-plain.

To figure out which reason is dominant, SEM, three-dimensional shape measurement and nanoindentation techniques were used for further study. The SEM photos of RS and NS are presented in Figure 14. RS has a rougher and more porous surface in comparison to NS. The special morphology of RS is the result of the residual old mortar during demolition.

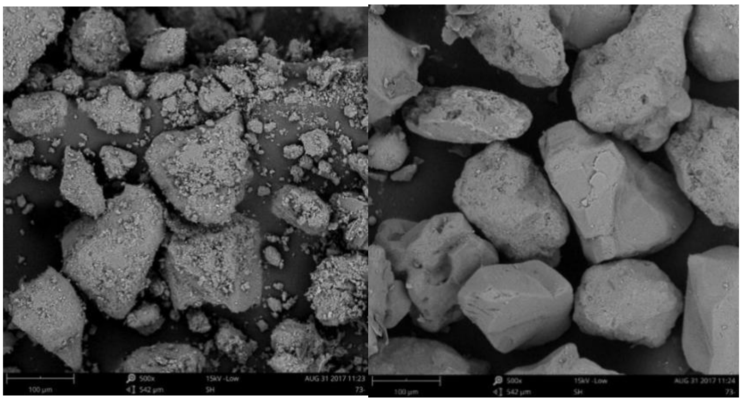

(**a**) (**b**)

**Figure 14.** SEM photo of NS and RS. (**a**) Recycled sand 12 grid; (**b**) natural sand 12 grid.

A three-dimensional shape measurement test was introduced to obtain 3D coordinate matrices of the fracture surface. Every data point in the coordinate matrix is linked to the adjacent points to build a triangle with the area of about 0.03 $mm^2$, as shown in Figure 15, which all together form a numerical fracture surface whose area can be easily calculated. Figure 16 shows a contour map of the RS-ECCs fracture surface cut by its base plane. The degree of warmth of color reflects the relative position and distance of a certain datum point to the base plane. As shown in Figure 17, most enhancement rates of the fracture area range from 3 to 7%, which are considered of little influence on the fracture energy at such a large scale. Therefore, the first explanation, i.e., a different pattern of crack propagation, is ruled out. The only explanation for the decrease in fracture toughness brought by RS replacement should be the weakened interface between the new cement binder and RS, which is consistent with the results given by Xiao et al. [38].

To support the above explanation, an insight into the microstructure of ECC was obtained by SEM. Figure 18 shows the microstructure characterization of NS-ECC and RS-ECC at 28 days. An obvious ITZ around the RS is observed, which is much thicker than that of NS-ECC. The weak ITZ makes cracks go through the aggregate with smaller stress and leads to a reduction in fracture toughness of the matrix. Figure 19 shows the average elastic modulus of a different phase of ECC. It can be seen due to the presence of the residual mortar that the gap in elastic modulus between sand and ITZ is much bigger than that of NS. The recycled sands act as “incompatible inclusion” in the matrix, causing serious stress concentration, which to some extent resembles the artificial flaws used to produce ECC [39,40]. Microcracks will be more easily generated and propagated in these regions, thus reducing the fracture toughness of composites.

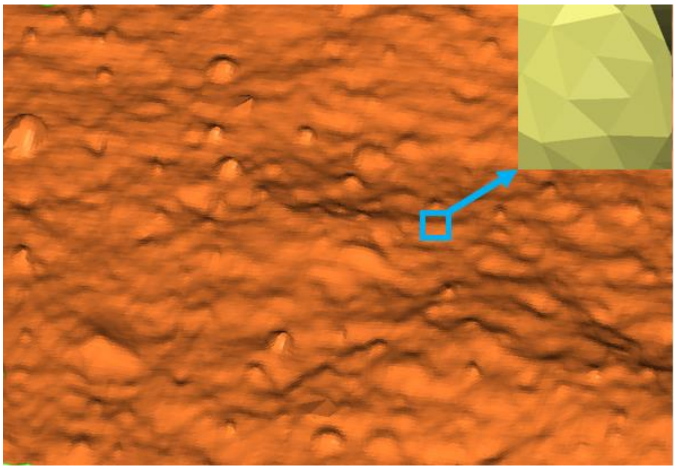

**Figure 15.** Three-dimensional photo of a fracture surface of RS-plain-20 grid.

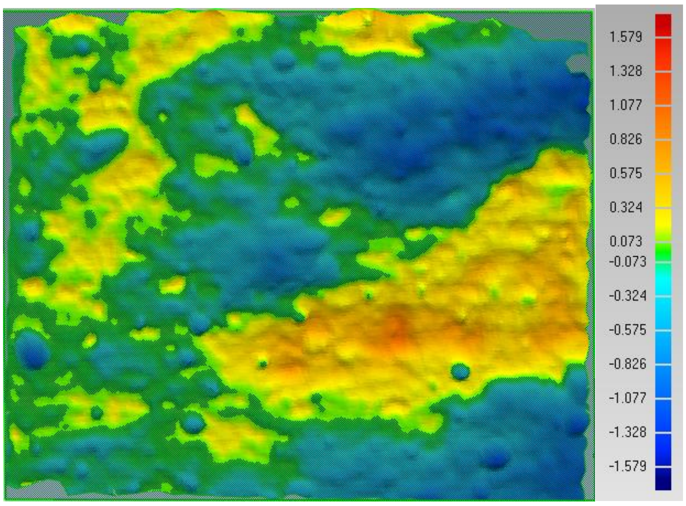


**Figure 16.** Contour map of a fracture surface of RS−plain cut by base plane (in mm).

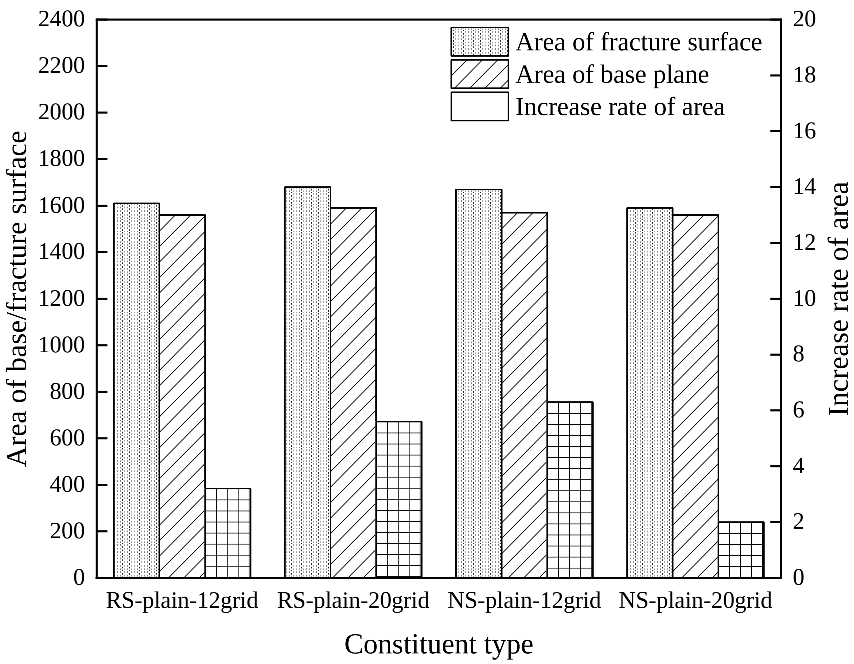


**Figure 17.** Parameters of the fracture surface.

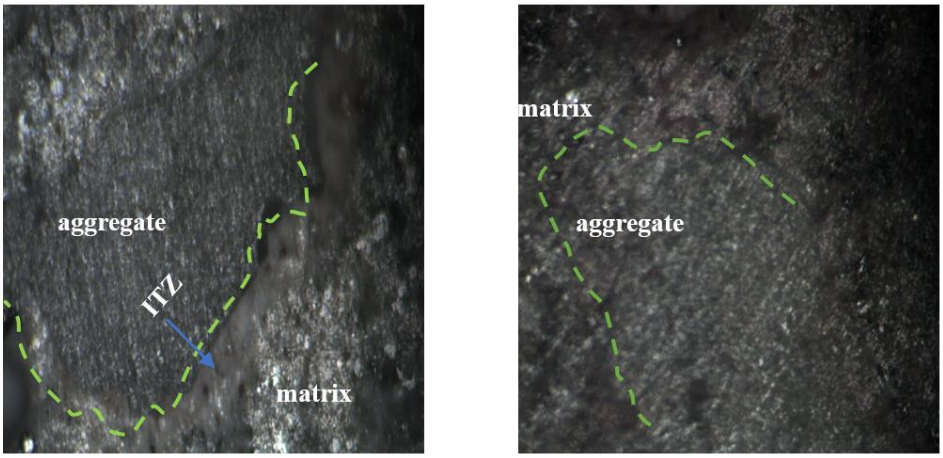


(**a**) (**b**)

**Figure 18.** Microstructure characterization of NS-ECC and RS-ECC. (**a**) RS-ECC-20 grid; (**b**) NS-ECC-12 grid.

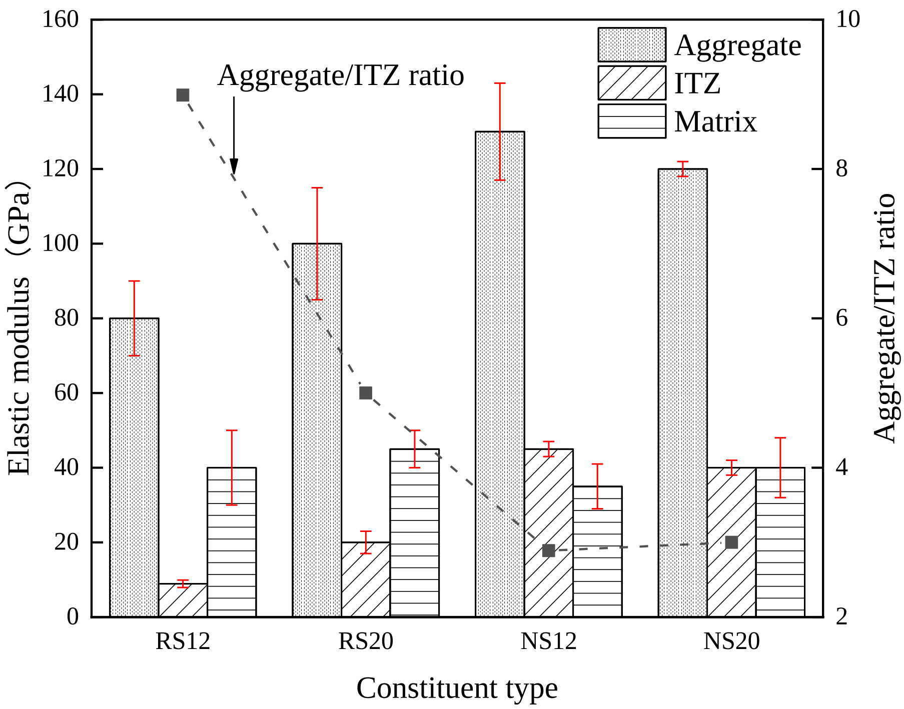


**Figure 19.** Average elastic modulus of different phases.

## 4. Conclusions

In the present research, the effect of recycled sand on the mechanical properties of engineered cementitious composites (ECC) was investigated. The strain-hardening mechanism of ECC with recycled sand was explored by the scanning electron microscope (SEM) and nano-indentation tests. The following conclusions could be obtained:

(1) The ECC with RS showed excellent tensile ductility with a tensile strain of 7%, which is greater than that of the ECC with NS. Furthermore, the incorporation of RS into ECC maintained the same tensile strength as that of NS-ECC.

(2) The compressive and flexural strengths of ECC were over 50 and 20 MPa. The addition of RS did not cause a significant loss of compressive and flexural strength, compared with that of ECC with NS.

(3) The addition of RS decreased the matrix toughness and kept the fiber-bridging capacity constant. The pseudo-strain-hardening (PSH) of RS-ECC showed the highest value, which could benefit tensile ductility. The main reason for this was that the old residual mortar around the RS increased the gap of elastic modulus between the sand and ITZ, which decreased the matrix toughness and improved the tensile ductility.

**Author Contributions:** Conceptualization, K.Y.; Investigation, X.J.; Supervision, Y.T. and J.Y.; Writing—original draft, Z.D. All authors have read and agreed to the published version of the manuscript.

**Funding:** This research received no external funding.

**Conflicts of Interest:** The authors declare no conflict of interest.

## References

1. Xiao, J.Z.; Qiang, C.B.; Nanni, A.; Zhang, K.J. Use of sea-sand and seawater in concrete construction: Current status and future opportunities. *Constr. Build. Mater.* **2017**, *155*, 1101–1111. [CrossRef]
2. Reyes-sánchezi, J.A.; Tenza-Abril, A.J.; Verdu, F.; Perales, J.A.R. Predicting modulus of elasticity of recycled aggregate concrete using nonlinear mathematical models. *Int. J. Comp. Meth. Exp. Meas.* **2018**, *6*, 703–715. [CrossRef]
3. Monteiro, P.J.M.; Miller, S.A.; Horvath, A. Towards sustainable concrete. *Nat. Mater.* **2017**, *16*, 698. [CrossRef] [PubMed]
4. Bourguiba, A.; Ghorbel, E.; Cristofol, L.; Dhaoui, W. Effects of recycled sand on the properties and durability of polymer and cement based mortars. *Constr. Build. Mater.* **2017**, *153*, 44–54. [CrossRef]
5. Xiao, J.Z.; Ma, Z.M.; Ding, T. Reclamation chain of waste concrete: A case study of shanghai. *Waste Manag.* **2015**, *48*, 334–343. [CrossRef] [PubMed]
6. Rahal, K. Mechanical properties of concrete with recycled coarse aggregate. *Build. Environ.* **2007**, *42*, 407–415. [CrossRef]
7. Corinaldesi, V. Mechanical and elastic behavior of concretes made of recycled-concrete coarse aggregates. *Constr. Build. Mater.* **2010**, *24*, 1616–1620. [CrossRef]
8. Pedro, D.J.; de Brito, J.; Evangelista, L. Influence of the use of recycled concrete aggregates from different sources on structural concrete. *Constr. Build. Mater.* **2014**, *71*, 141–151. [CrossRef]
9. Ferro, G.A.; Spoto, C.; Tulliani, J.M.; Restuccia, L. Mortar made of recycled sand from C&D. *Procedia Eng.* **2015**, *109*, 240–247.
10. Khatib, J.M. Properties of concrete incorporating fine recycled aggregate. *Cem. Concr. Res.* **2005**, *35*, 763–769. [CrossRef]
11. Evangelista, L.; de Brito, J. Mechanical behaviour of concrete made with fine recycled concrete aggregates. *Cem. Concr. Compos.* **2007**, *29*, 397–401. [CrossRef]
12. Khoshkenari, A.G.; Shafigh, P.; Moghimi, M.; Mahmud, H.B. The role of 0–2 mm fine recycled concrete aggregate on the compressive and splitting tensile strengths of recycled concrete aggregate concrete. *Mater. Des.* **2014**, *64*, 345–354. [CrossRef]
13. Pereira, P.; Evangelista, L.; de Brito, J. The effect of superplasticisers on theworkability and compressive strength of concrete made with fine recycledconcrete aggregates. *Constr. Build. Mater.* **2012**, *28*, 722–729. [CrossRef]
14. Fan, C.; Huang, R.; Hwang, H.; Chao, S. Properties of concrete incorporating fine recycled aggregates from crushed concrete wastes. *Constr. Build. Mater.* **2016**, *112*, 708–715. [CrossRef]
15. Carro-López, D.; Gónzález-Fonteboa, F.; Martínez, A.; Gónzález, T.; de Brito, J.; Varela-Puga, F. Proportioning, microstructure and fresh properties of self-compacting concrete with recycled sand. *Procedia Eng.* **2017**, *171*, 645–657. [CrossRef]
16. Yu, K.; Mcgee, W.; Ng, T.Y.; Zhu, H.; Li, V.C. 3D-printable engineered cementitious composites (3DP-ECC): Fresh and hardened properties. *Cem. Concr. Res.* **2021**, *143*, 106388. [CrossRef]
17. Ye, J.; Cui, C.; Yu, J.; Yu, K.; Xiao, J. Fresh and anisotropic-mechanical properties of 3D printable ultra-high ductile concrete with crumb rubber. *Compos. Part B Eng.* **2021**, *211*, 108639. [CrossRef]
18. Liao, Q.; Su, Y.; Yu, J.; Yu, K. Torsional behavior of BFRP bars reinforced engineered cementitious composites beams without stirrup. *Eng. Struct.* **2022**, *268*, 114748. [CrossRef]
19. Liao, Q.; Su, Y.; Yu, J.; Yu, K. Compression-shear performance and failure criteria of seawater sea-sand engineered cementitious composites with polyethylene fibers. *Constr. Build. Mater.* **2022**, *345*, 128386. [CrossRef]
20. Li, V.C. Engineered cementitious composites-tailored composites through micromechanical modelling. In *Fiber Reinforced Concrete: Present and the Future*; Canadian Society for Civil Engineering: Montreal, QC, Canada, 1998; pp. 64–97.
21. Cai, Z.; Liu, F.; Yu, J.; Yu, K.; Tian, L. Development of ultra-high ductility engineered cementitious composites as a novel and resilient fireproof coating. *Constr. Build. Mater.* **2021**, *288*, 123090. [CrossRef]
22. Sahmaran, M.; Li, M.; Li, V.C. Transport Properties of Engineered Cementitious Composites under Chloride Exposure. *ACI Mater. J.* **2007**, *104*, 303–310.
23. Qian, S.Z.; Li, V.C. Headed Anchor/Engineered Cementitious Composites (ECC) Pullout Behavior. *J. Adv. Concr. Technol.* **2011**, *9*, 339–351. [CrossRef]
24. Qian, S.Z.; Li, V.C.; Zhang, H.; Keoleian, G.A. Life cycle analysis of pavement overlays made with Engineered Cementitious Composites. *Cem. Concr. Compos.* **2013**, *35*, 78–88. [CrossRef]

25. Dong, Z.; Tan, H.; Yu, J.; Liu, F. A feasibility study on Engineered cementitious Composites mixed with coarse aggregate. *Constr. Build. Mater.* **2022**, *350*, 128587. [CrossRef]
26. Sahmaran, M.; Lachemi, M.; Li, V.C. Assessing the Durability of Engineered Cementitious Composites Under Freezing and Thawing Cycles. *J. ASTM Int.* **2009**, *6*, 102406–102419.
27. Kanda, T.; Li, V.C. New micromechanics design theory for pseudo strain hardening cementitious composite. *ASCE J. Eng. Mech.* **1999**, *125*, 373–381. [CrossRef]
28. Wang, S.; Li, V.C. Tailoring of pre-existing flaws in ECC matrix for saturated strain hardening. In Proceedings of the Fifth International Conference on Fracture Mechanics of Concrete and Concrete Structures, Vail, CO, USA, 12–16 April 2004; pp. 1005–1012.
29. Zhang, Z.G.; Qian, S.Z.; Ma, H. Investigating mechanical properties and self-healing behavior of micro-cracked ECC with different volume of fly ash. *Constr. Build. Mater.* **2014**, *52*, 17–23. [CrossRef]
30. Zhang, Z.G.; Ma, H.; Qian, S.Z. Investigation on Properties of ECC Incorporating Crumb Rubber of Different Sizes. *J. Adv. Concr. Technol.* **2015**, *13*, 241–251. [CrossRef]
31. Zhang, Z.G.; Zhang, Q.; Qian, S.Z.; Li, V.C. Low E-Modulus Early Strength Engineered Cementitious Composites Material Development for Ultrathin Whitetopping Overlay. *Transp. Res. Rec. J. Transp. Res. Board* **2015**, *2481*, 41–47. [CrossRef]
32. Lepech, M.D.; Li, V.C. Application of ECC for bridge deck link slabs. *Mater. Struct.* **2009**, *42*, 1185–1195. [CrossRef]
33. Sahmaran, M.; Yücel, H.E.; Demirhan, S.; Arık, M.T.; Li, V.C. Combined Effect of Aggregate and Mineral Admixtures on Tensile Ductility of Engineered Cementitious Composites. *ACI Mater. J.* **2009**, *109*, 11.
34. Xu, S.; Reinhardt, H.W. Determination of double-K criterion for crack propagation in quasi-brittle fracture, Part II: Analytical evaluating and practical measuring methods for three-point bending notched beams. *Int. J. Fract.* **1999**, *98*, 151–177. [CrossRef]
35. Yang, Y.Z.; Yao, Y.; Zhu, Y. Effects of Gradation of Sand on the Mechanical Properties of Engineered Cementitious Composites. *Adv. Mater. Res.* **2011**, *250*, 374–378. [CrossRef]
36. Chen, B.; Li, J. Effect of aggregate on the fracture behavior of high strength concrete. *Constr. Build. Mater.* **2004**, *18*, 585–590. [CrossRef]
37. Li, Y.; Li, J.Q. Relationship between fracture area and tensile strength of cement matrix with supplementary cementitious materials. *Constr. Build. Mater.* **2015**, *79*, 223–228. [CrossRef]
38. Li, W.; Xiao, J.; Sun, Z.; Kawashima, S.; Shah, S.P. Interfacial transition zones in recycled aggregate concrete with different mixing approaches. *Constr. Build. Mater.* **2012**, *35*, 1045–1055. [CrossRef]
39. Ollivier, J.P.; Maso, J.C.; Bourdette, B. Interfacial transition zone in concrete. *Adv. Cem. Based Mater.* **1995**, *2*, 30–38. [CrossRef]
40. Bremner, T.W.; Holm, T.A. Elastic Compatibility and the Behavior of Concrete. *J. Proc.* **1986**, *83*, 244–250.